# Insight into the Microstructural Characterization of Ferritic Steels Using Micromagnetic Parameters

V. MOORTHY, S. VAIDYANATHAN, BALDEV RAJ, T. JAYAKUMAR, and B.P. KASHYAP

The influence of tempering-induced microstructural changes on the micromagnetic parameters such as magnetic Barkhausen emission (MBE), coercive force ($H_c$), residual induction ($B_r$), and maximum induction ($B_{max}$) has been studied in 0.2 pct carbon steel, 2.25Cr-1Mo steel, and 9Cr-1Mo steel. It is observed that, after short tempering, the micromagnetic parameters show more or less linear correlation with hardness, which is attributed to the reduction in dislocation density, but long-term tempering produces nonlinear behavior. The variation in each of these parameters with tempering time has been explained based on the changes in the size and distribution of ferrite laths/grains and precipitates. It has been shown that the individual variation in the microstructural features such as size and distribution of laths/grains and precipitates during tempering can be clearly identified by the MBE parameters, which is not possible from the hysteresis loop parameters ($H_c$ and $B_r$). It is also shown that the MBE parameters can not only be used to identify different stages of tempering but also to quantify the average size of laths/grains and second-phase precipitates.

## I. INTRODUCTION

MANY investigations over the past five decades prove that micromagnetic parameters such as coercive force ($H_c$), residual induction ($B_r$), maximum permeability ($\mu_{max}$), maximum induction ($B_{max}$), magnetic Barkhausen emission (MBE), *etc.*, can be used to predict the microstructural state as well as the mechanical properties such as hardness, yield strength, tensile strength, *etc.*, in ferromagnetic materials.[1–4] It has been found that the microstructural features such as dislocations, grain boundaries, second-phase precipitates, *etc.*, strongly affect the domain wall movement and, hence, the magnetic parameters.[1–12] Quantitative relations have been obtained between grain size and magnetic parameters ($H_c$ and MBE).[l,3,4,7,8] Similarly, $H_c$ has been related with average size and volume fraction of inclusions and second-phase precipitates. [l,9–12] However, the theory of ferromagnetism is not able to explain the observed quantitative relationship between the magnetic and microstructural parameters, particularly in tempered structural steels.[13] For example, a difference of more than five times has been observed between the actual and theoretically predicted values of coercive force in 0.2 pct carbon steel.[14]

Normally, when a steel is subjected to heat treatment or exposed to high temperature, microstructural features evolve in a complex manner. For example, the dislocations dominate the microstructure in the quenched and early stage of tempering, whereas the variations in grain size and carbide precipitation dominate the later stage of tempering/aging. The magnetization process and, hence, the micromagnetic properties for a particular microstructural state are influenced by the synergistic interactions of domain walls with these microstructural features. However, in most of the studies carried out to date, the micromagnetic parameters are correlated with only one microstructural feature at a time, ignoring the effects of other features. For example, the magnetic properties are correlated with grain size without considering the effect of precipitates. Similarly, they are related to the size and/or volume fraction of precipitates without taking into account the effect of grain boundaries.

Even though the micromagnetic parameters are found to be influenced by the variations in the size and distribution of both grains and precipitates in tempered steels, the individual variation during various stages of tempering/aging has not yet been resolved. Recently, the present authors have established the influence of different tempered microstructures on the MBE in 0.2 pct carbon steel, 2.25Cr-1Mo steel, and 9Cr-1Mo steel, and shown[15,16] that the MBE behavior changes systematically from a single peak to two peaks with increasing tempering time. This has been explained[15,16] using a two-stage magnetization process, considering the lath/grain boundaries and second-phase particles as the two major obstacles to the domain wall motion, which would vary with tempering time, while the matrix crystal structure, chemical composition, and dislocation density remain constant beyond a certain extent of tempering. This study mainly deals with the comparison between the variations in the hysteresis loop parameters, MBE parameters, and hardness during tempering to understand the influence of microstructural evolution during tempering and to identify the best magnetic parameter for effective microstructural characterization.

## II. EXPERIMENTAL

The 0.2 pct carbon steel, 2.25Cr-1Mo steel, and 9Cr-1Mo steel were selected in order to observe the effect of precipitation of single-type carbides (as in carbon steel) and different types of carbides (as in Cr-Mo steels) during tempering. Also, because these Cr-Mo steels are extensively used for high-temperature applications in steam generator systems in power industries, they undergo degradation of the microstructure and mechanical properties. The chemical

V. MOORTHY, Scientific Officer "E," S. VAIDYANATHAN, Scientific Officer "F," BALDEV RAJ, Director, and T. JAYAKUMAR, Scientific Officer "G," are with the Metallurgy and Materials Group, Indira Gandhi Centre for Atomic Research, Kalpakkam-603 102, India. B.P. KASHYAP, Professor, is with the Department of Metallurgical Engineering and Materials Science, Indian Institute of Technology, Bombay-400 076, India.

Manuscript submitted April 27, 1999.

**Table I. Chemical Composition (Weight Percent) of Carbon Steel, 2.25Cr-1Mo Steel, and 9Cr-1Mo Steel**

| Steel | Cr | Mo | Mn | C | P | Si | S | Ni | Fe |
|---|---|---|---|---|---|---|---|---|---|
| Carbon steel | — | — | 0.120 | 0.22 | 0.003 | 0.015 | 0.045 | 0.02 | balance |
| 2.25Cr-1Mo steel | 2.210 | 0.94 | 0.480 | 0.11 | 0.007 | 0.190 | — | — | balance |
| 9Cr-1Mo steel | 8.240 | 0.96 | 0.360 | 0.07 | 0.021 | 0.265 | — | — | balance |

composition (wt pct) of the carbon steel, 2.25Cr-1Mo steel, and 9Cr-1Mo steel used in this study is given in Table I. The carbon steel used in this study is of commercial grade and the Cr-Mo steels are of nuclear grade with low inclusion content. The samples having 150-mm length were cut from the 12-mm-diameter rods and were heat treated as follows. The carbon steel specimens were solutionized at 1223 K for 1 hour followed by water quenching and then tempered at 873 K for 0.5, 1, 5, 15, 25, and 100 hours. The 2.25Cr-1Mo steel rods were normalized at 1373 K for 1 hour and then tempered at 923 K for 2, 10, 20, 50, 200, and 500 hours. The heat treatments for 2.25Cr-1Mo steel were selected based on the carbide stability diagram developed by Becker and Nutting[19] in order to get different combinations of carbide precipitates. The 9Cr-1Mo steel rods were normalized at 1373 K and then tempered at 923 K for 2, 10, 50, 200, and 500 hours. The 20-mm-thick 9Cr-1Mo steel plate was normalized at 1223 K for 15 minutes followed by air cooling and tempered at 1023 K for 2 hours followed finally by air cooling. For the purpose of metallographic examinations, 10-mm-thick samples were cut from these steel rods and plate and then heat treated along with each test specimen.

Following the heat treatments, the steel rods were machined to 10-mm diameter at a low feed rate with a high cooling rate in order to avoid machining effect and residual stresses. The 10-mm-diameter rods were used for studying the effect of tempered microstructures. The microstructural evolution at different stages of tempering has been studied using light optical, scanning electron, and transmission electron microscopes by standard procedures.

The experimental procedure for the measurement of magnetic hysteresis loop and MBE are given in the authors' previous article.[16] The plots of the magnetic induction and the root-mean-square (RMS) voltage of the MBE *vs* current applied to the electromagnetic yoke were used for analysis. The applied magnetic field measured at the center of the yoke without the specimen is linearly proportional to the current applied to the yoke. Hence, the coercive force (given in terms of applied magnetic field, *A*/*m*) corresponds to the current applied to the yoke when the magnetic induction becomes zero and the residual induction corresponds to zero current applied to the yoke. The MBE peak position is also given in terms of current (*A*) applied to the yoke.

## III. RESULTS AND DISCUSSION

### A. *Microstructural Evolution during Tempering*

Earlier studies[17,18] have shown that the tempering of carbon steels with carbon content greater than 0.2 pct at temperatures greater than 673 K causes the recovery and recrystallization of martensite into ferrite and spheroidization and growth of cementite. Figures 1(a) and (b) show typical optical photomicrographs of 0.2 pct carbon steel samples tempered at 873 K for 5 and 100 hours, respectively,

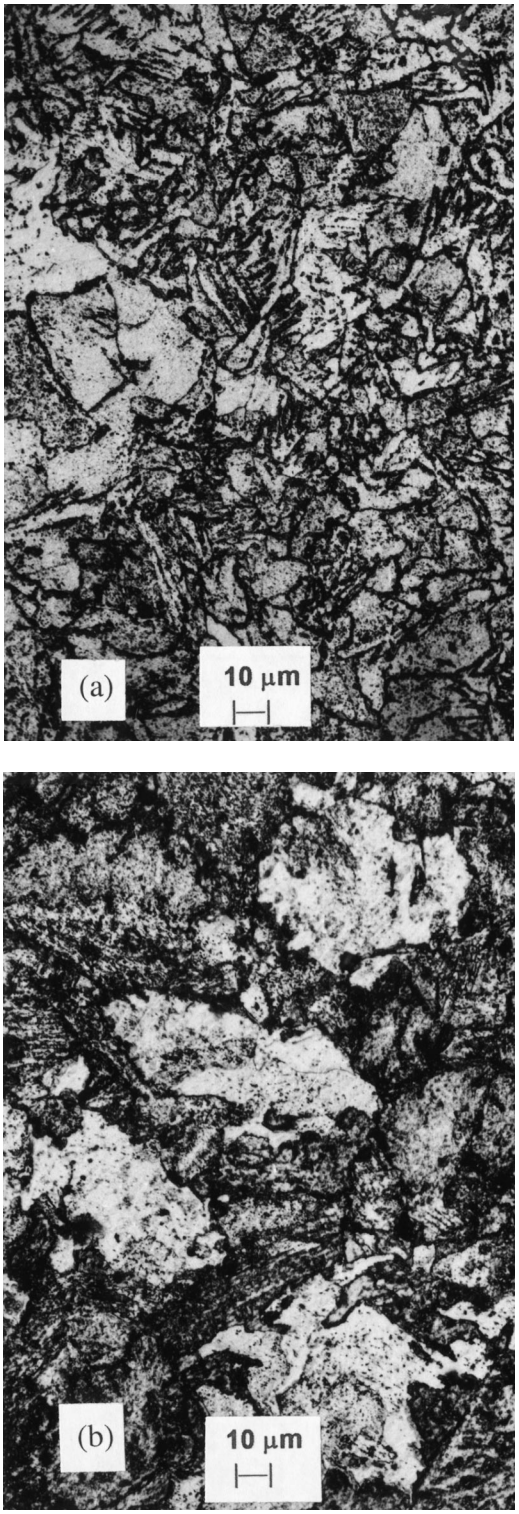


Fig. 1—Optical micrographs of 0.2 pct carbon steel samples tempered at 873 K for (*a*) 5 h and (*b*) 100 h.

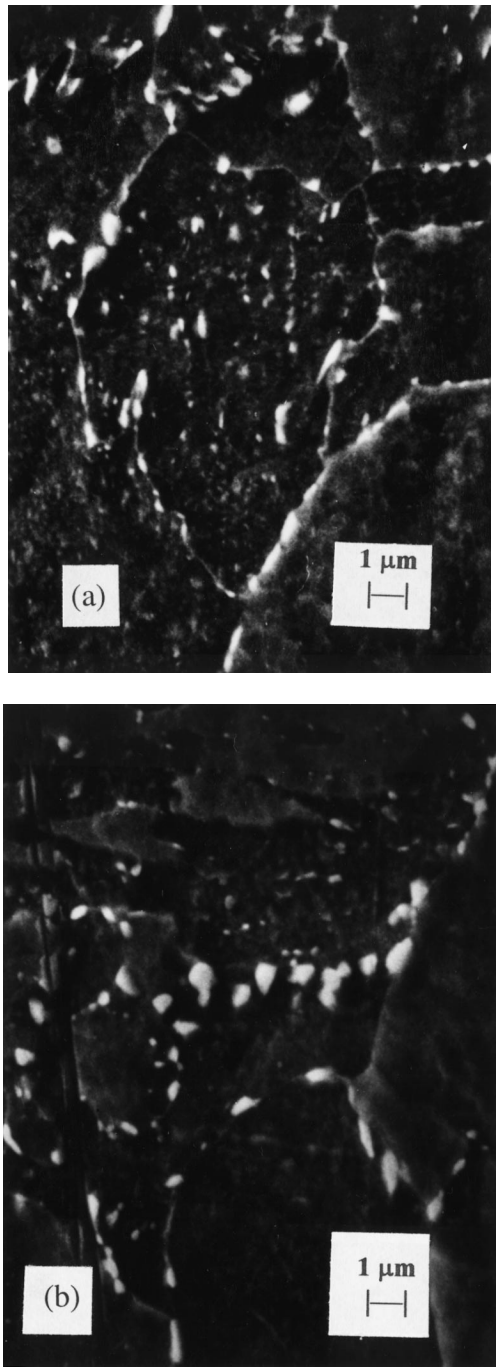


Fig. 2—Scanning electron micrographs of 0.2 pct carbon steel samples tempered at 873 K for (*a*) 5 and (b) 100 h.

which clearly shows the polygonization of laths and grain coarsening with an increase in tempering time. Figures 2(a) and (b) are typical scanning electron microscope photomicrographs of 0.2 pct carbon steel samples tempered at 873 K for 5 and 100 hours, which clearly show the increase in the average cementite size with tempering time. Table II shows the average grain size and cementite size in different tempered 0.2 pct carbon steel samples.

Extensive studies[19,20,21] on 2.25Cr-1Mo steel using a transmission electron microscope (TEM) have well established the microstructural changes during tempering. Figures 3(a) and (b) show typical optical micrographs of the 2.25Cr-1Mo steel samples tempered at 923 K for 10 and 500 hours respectively, which clearly show the polygonization of ferrite laths and the grain coarsening. Figures 4(a) and (b) show TEM micrographs of the carbon extraction replica for 2.25Cr-1Mo steel samples tempered at 923 K for 50 and 500 hours. This shows the dense distribution of fine needle-like $M_2C$ precipitates after 50 hours of tempering (Figure 4(a)), which dissolves and forms $M_{23}C_6$ after 500 hours of tempering (Figure 4(b)). An inset in Figure 4(b) shows the $\langle \bar{1}11 \rangle$ selected area diffraction (SAD) pattern of a carbide particle, which identifies it as $M_{23}C_6$-type carbide.

**Table II. Average Size of Grains and Cementite Particles in Different Tempered 0.2 Pct Carbon Steel Samples**

| Tempering Time (h) | Average Size of Grains ($\mu$m) | Average Size of Cementite Particles ($\mu$m) |
|---|---|---|
| 1 | 3.7 | 0.13 |
| 5 | 5.6 | 0.17 |
| 15 | 8.9 | 0.26 |
| 25 | 10.7 | 0.34 |
| 100 | 21.5 | 0.46 |

Saroja *et al.*[23,24] and Sanderson[22] have studied in detail the effect of tempering on the microstructure of the 9Cr-1Mo steel using a TEM. Figures 5(a) and (b) show optical micrographs of the 9Cr-1Mo steel samples tempered at 923 K for 10 and 500 hours, respectively, which show the polygonization of ferrite laths during tempering. Figures 6(a) and (b) show the TEM micrographs of the carbon extraction replica for 9Cr-1Mo steel samples tempered at 923 K for 50 and 500 hours. The inset in Figure 6(a) shows a $\langle \bar{2}10 \rangle$ electron microdiffraction pattern of a carbide particle in the 50 hour tempered sample, which identifies it as $Cr_2X$-type carbide. In the 9Cr-1Mo steel sample tempered for 500 hours, the number density of $M_2X$ has drastically reduced, and the $M_{23}C_6$ type was predominant (Figure 6(b)). In the case of Cr-Mo steels, the presence of a fine, dense distribution of $M_2X$-type precipitates would retard lath coarsening and would delay the kinetics of tempering as compared with carbon steel.[19–24] This kind of stabilization of microstructure in Cr-Mo steels makes them attractive for high-temperature applications where creep resistance is important.

It is evident from these optical, scanning electron, and transmission electron microscope studies that the observed microstructural changes due to tempering in these steels are in agreement with those reported in the literature.[17–24] The average size of laths/grains and carbide particles increases and the size distribution of carbides broadens as the tempering progresses. Therefore, it is expected that the variations in size and distribution of ferrite laths/grains and carbides are the major factors that would influence the magnetization process and, hence, the micromagnetic parameters.

### B. *Influence of Tempered Microstructures on the Hardness and the Micromagnetic Parameters*

Figures 7(a) through (f), 8(a) through (f), and 9(a) through (f) show the variations in hardness, the position and height of the MBE single peak, peak 1 and peak 2, coercive force ($H_c$), residual induction ($B_r$), and maximum flux density

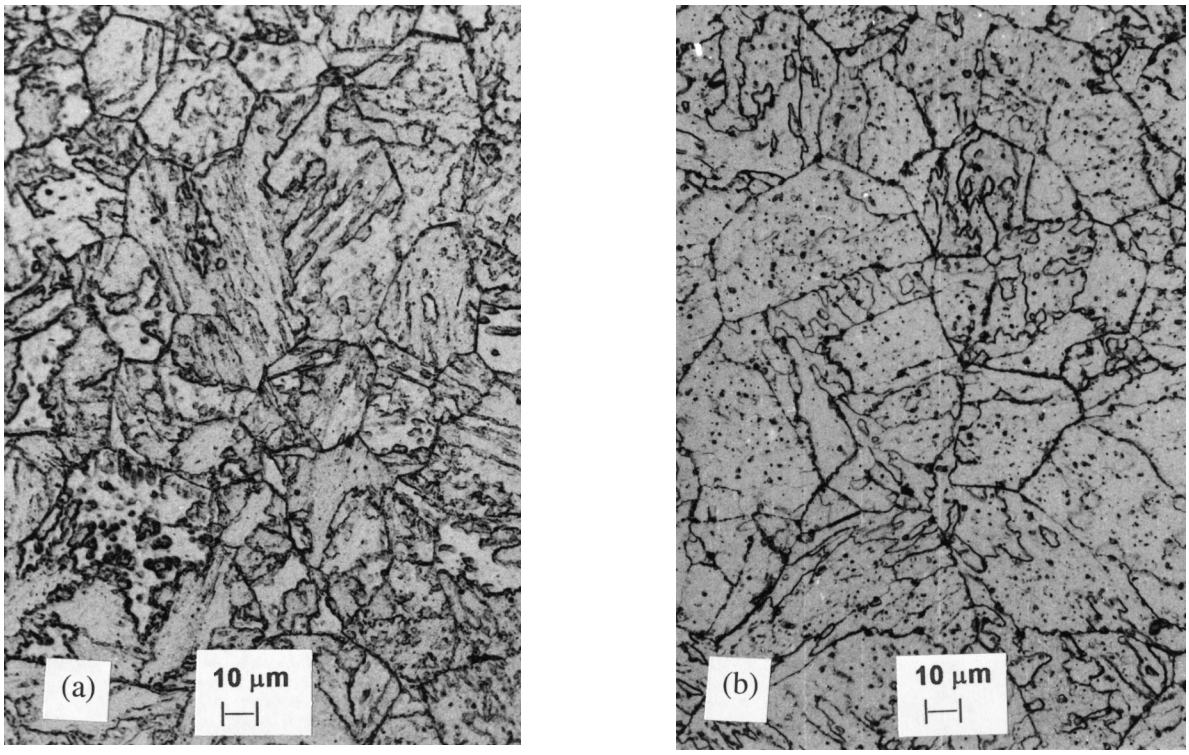


Fig. 3—Optical micrographs of 2.25Cr-1Mo steel samples tempered at 923 K for (*a*) 10 h and (*b*) 500 h.

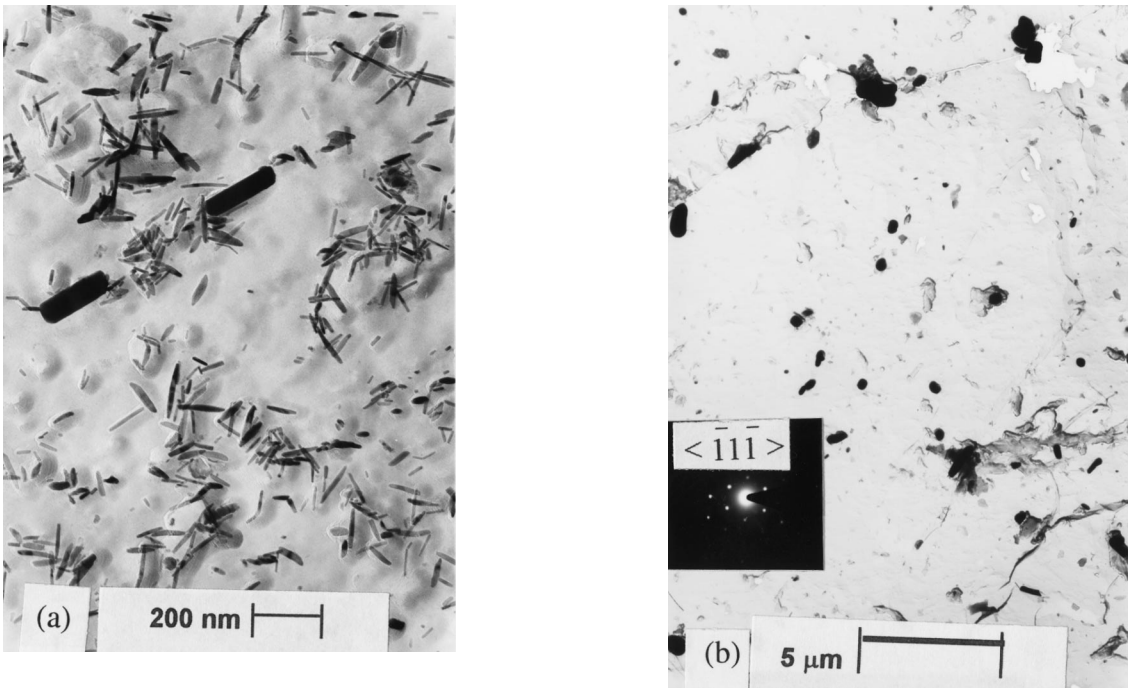


Fig. 4—TEM micrographs of the carbon extraction replica for 2.25Cr-1Mo steel samples tempered 923 K for (*a*) 50 h and (*b*) 500 h. Inset in (b) shows the $\langle \bar{1}\bar{1}1 \rangle$ SAD pattern of a carbide particle, which identifies it as $M_{23}C_6$ type.

($B_{max}$) as a function of tempering time for the 0.2 pct carbon, 2.25Cr-1Mo, and 9Cr-1Mo steels, respectively.

1. *Effect of tempering on hardness*

It can be observed from Figures 7(a), 8(a), and 9(a) that the hardness drops rapidly after short-time tempering, which is attributed to the reduction in dislocation density due to dislocation annihilation. It is known that, on tempering the quenched materials, the secondary hardening is well pronounced only in the presence of coherent second-phase precipitates, as in the case of Al-Cu alloys, 17-4PH steel, maraging steel, *etc.*, which is due to the lattice coherency

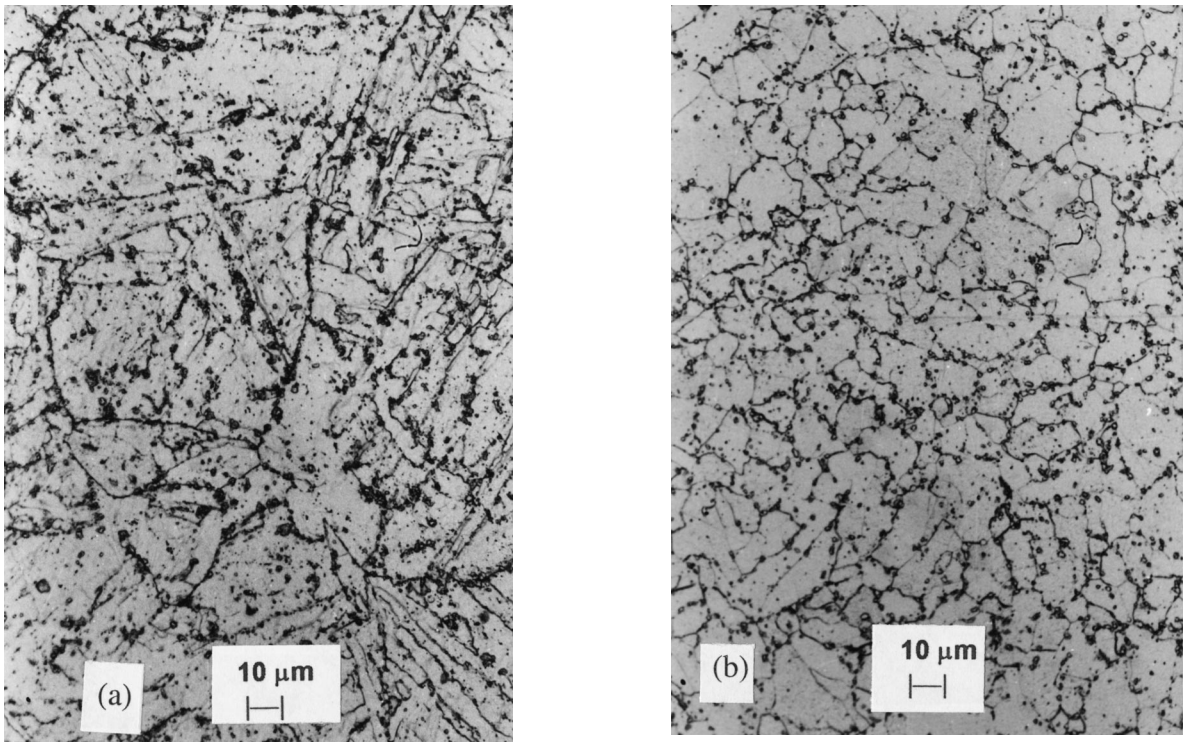


Fig. 5—Optical micrographs of 9Cr-1Mo steel samples tempered at 923 K for (*a*) 10 and (*b*) 500 h.

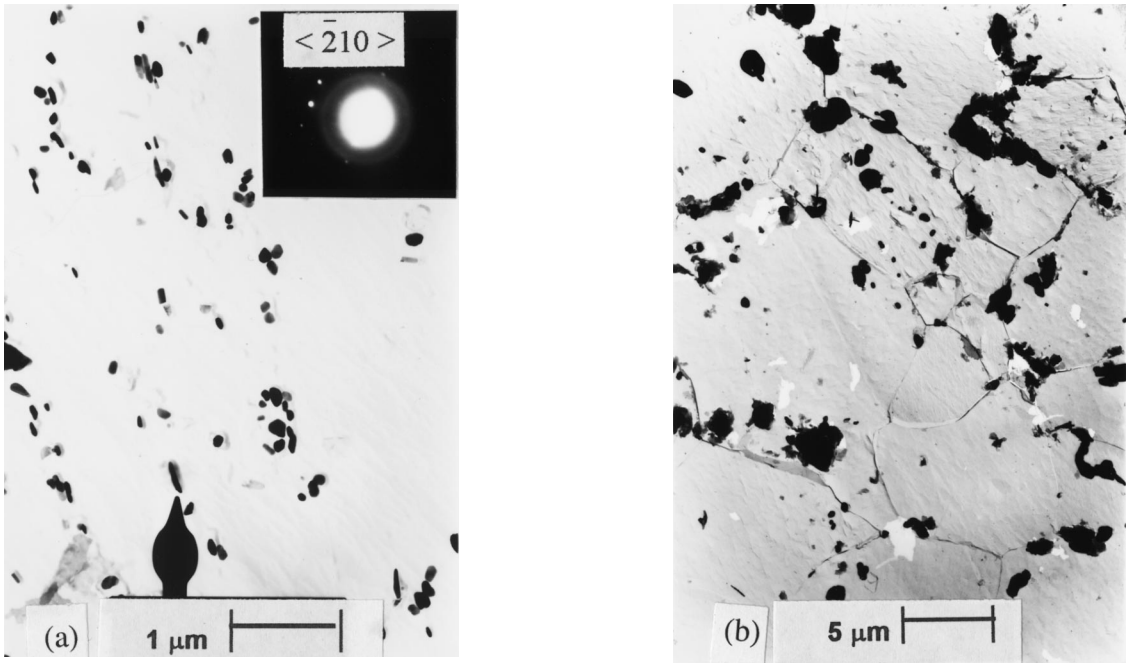


Fig. 6—TEM micrographs of the carbon extraction replica for 9Cr-1Mo steel samples tempered 923 K for (*a*) 50 and (*b*) 500 h. Inset in (a) shows the ⟨2̄10⟩ electron microdiffraction pattern of a carbide particle, which identifies it as $Cr_2X$ type.

strain. The cementite in carbon steel is not a coherent precipitate and, hence, no secondary hardening occurs on tempering; *i.e.*, beyond 1 hour of tempering, the hardness decreases gradually (Figure 7(a)). In the case of the 2.25Cr-1Mo steel, Baker and Nutting[19] showed that the fine and dense precipitation of needle-like $M_2C$ precipitates retards the lath coarsening and polygonization, thereby leading to a slight secondary hardening. Parameswaran *et al.*[20] showed from the streaking of an electron SAD pattern that the secondary hardening in 2.25Cr-1Mo steel is due to the coherency strain produced by the $M_2C$ precipitates. In the case of 9Cr-1Mo steel also,[21,24] the fine precipitation of $M_2X$ has been found to hamper the drop in the hardness values. It can be observed from Figures 8(a) and 9(a) that, in the case of Cr-Mo steels,

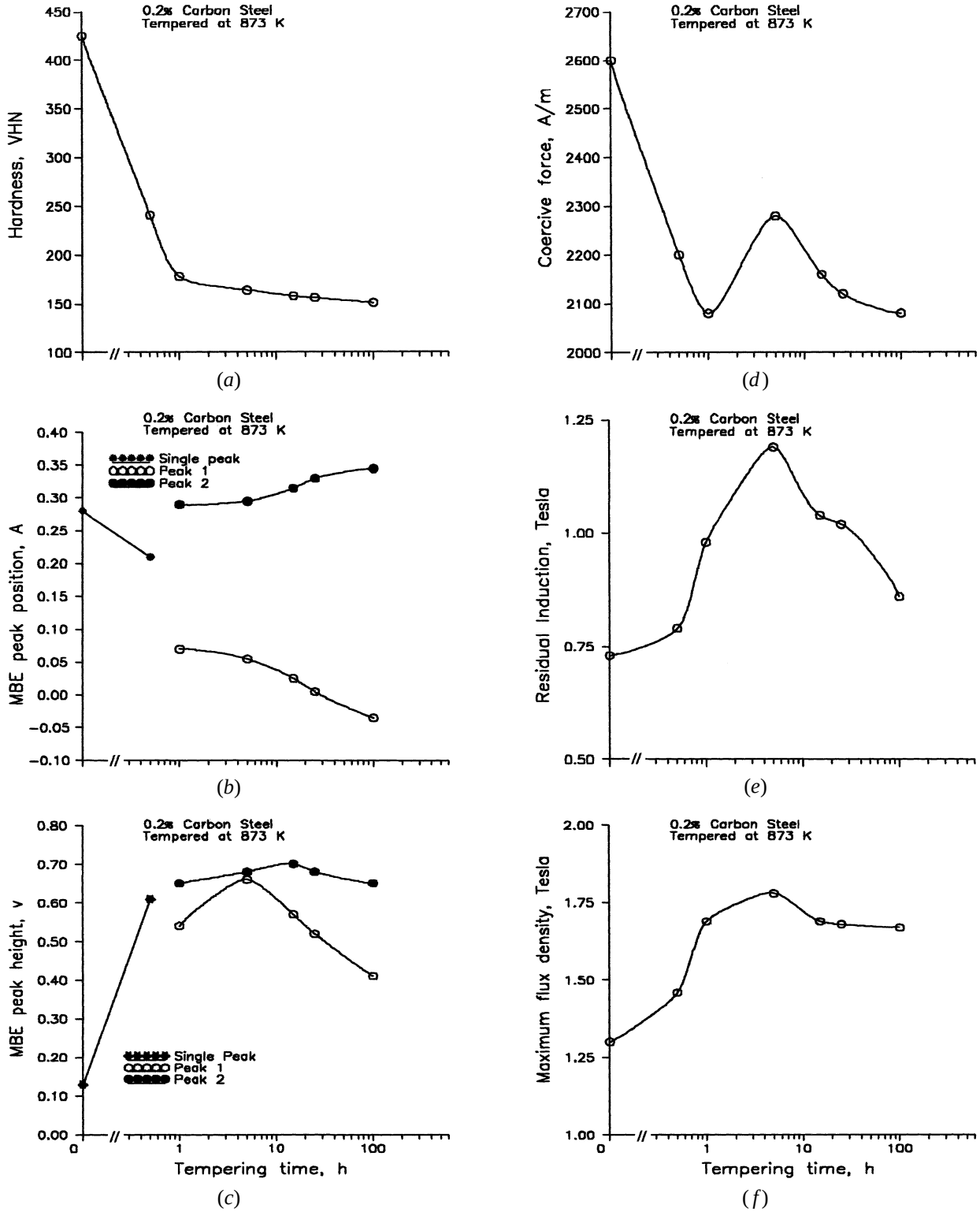


Fig. 7—The variation in (*a*) hardness, (*b*) MBE peak 1 and peak 2 positions, (*c*) MBE peak 1 and peak 2 height values, (*d*) coercive force ($H_c$), (*e*) residual induction ($B_r$), and (*f*) maximum flux density ($B_{max}$) as a function of tempering time for 0.2 pct carbon steel.

the reduction in hardness is delayed after short tempering (after 10 hours in 2.25Cr-1Mo steel and after 2 hours in 9Cr-1Mo steel). This can be attributed to the precipitation of coherent $M_2X$ precipitates in the early stages of tempering. On further tempering, the hardness values drop significantly (after 50 hours in 2.25Cr-1Mo steel and after 200 hours in 9Cr-Mo steel). This can be ascribed to the loss of coherency due to the coarsening of $M_2X$ precipitates on further tempering. The presence of dense incoherent $M_2X$ precipitates would resist the lath/grain coarsening by pinning the bound-

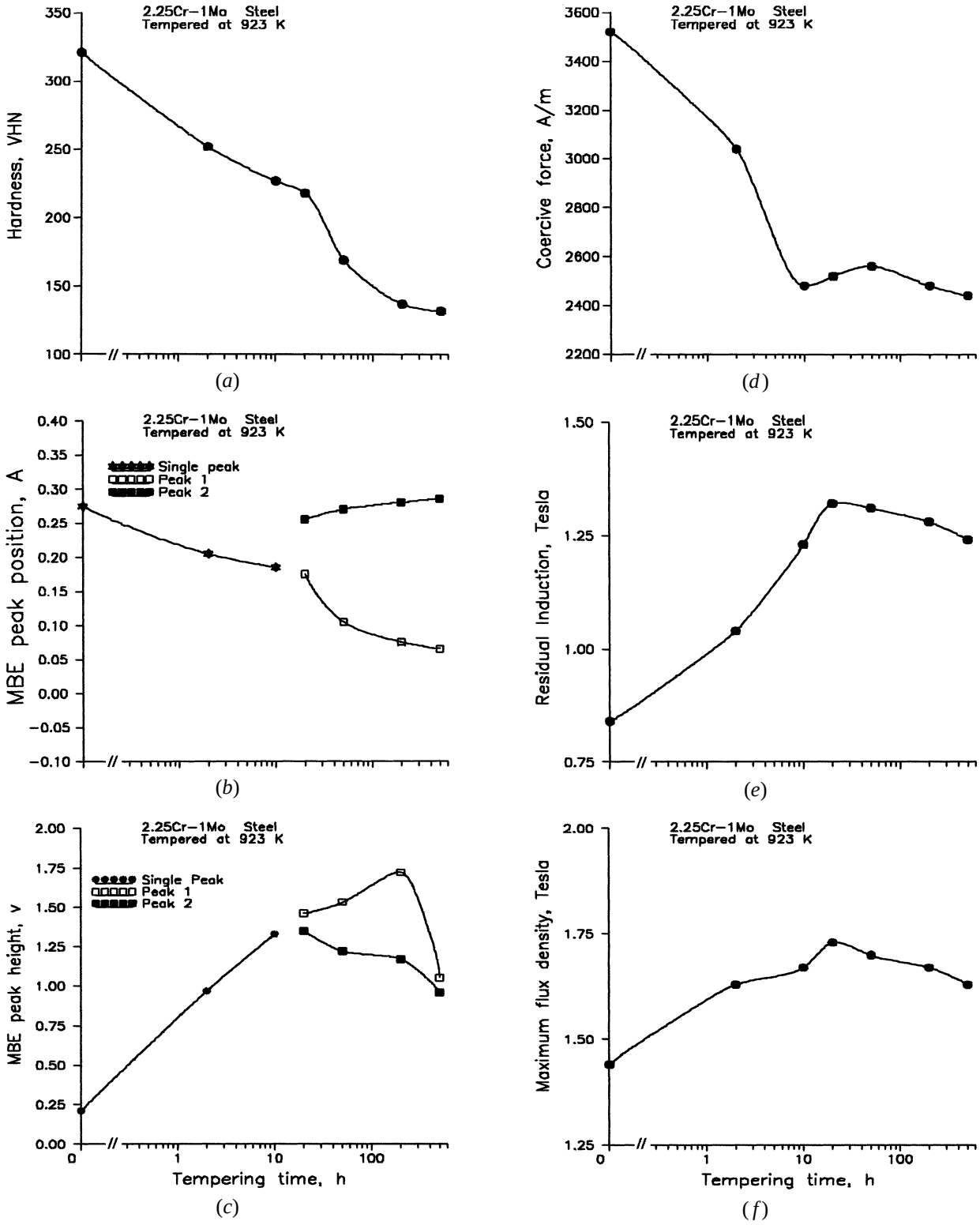


Fig. 8—The variation in (*a*) hardness, (*b*) MBE peak 1 and peak 2 positions, (*c*) MBE peak 1 and peak 2 height values, (*d*) coercive force ($H_c$), (*e*) residual induction ($B_r$), and (*f*) maximum flux density ($B_{max}$) as a function of tempering time for 2.25Cr-1Mo steel.

aries.[21,24] Hence, the dissolution of $M_2X$ precipitates after prolonged tempering would lead to rapid polygonization of ferrite laths and coarsening of secondary carbides. However, this is not clearly reflected in the hardness variation (Figures 8(a) and 9(a)).

2. *Effect of tempering on the MBE behavior*

The systematic changes in the MBE behavior from a single peak to two peaks with an increase in tempering time (Figures 7(b) and (c), 8(b) and (c), and 9(b) and (c)) have been explained earlier using a two-stage magnetization pro-

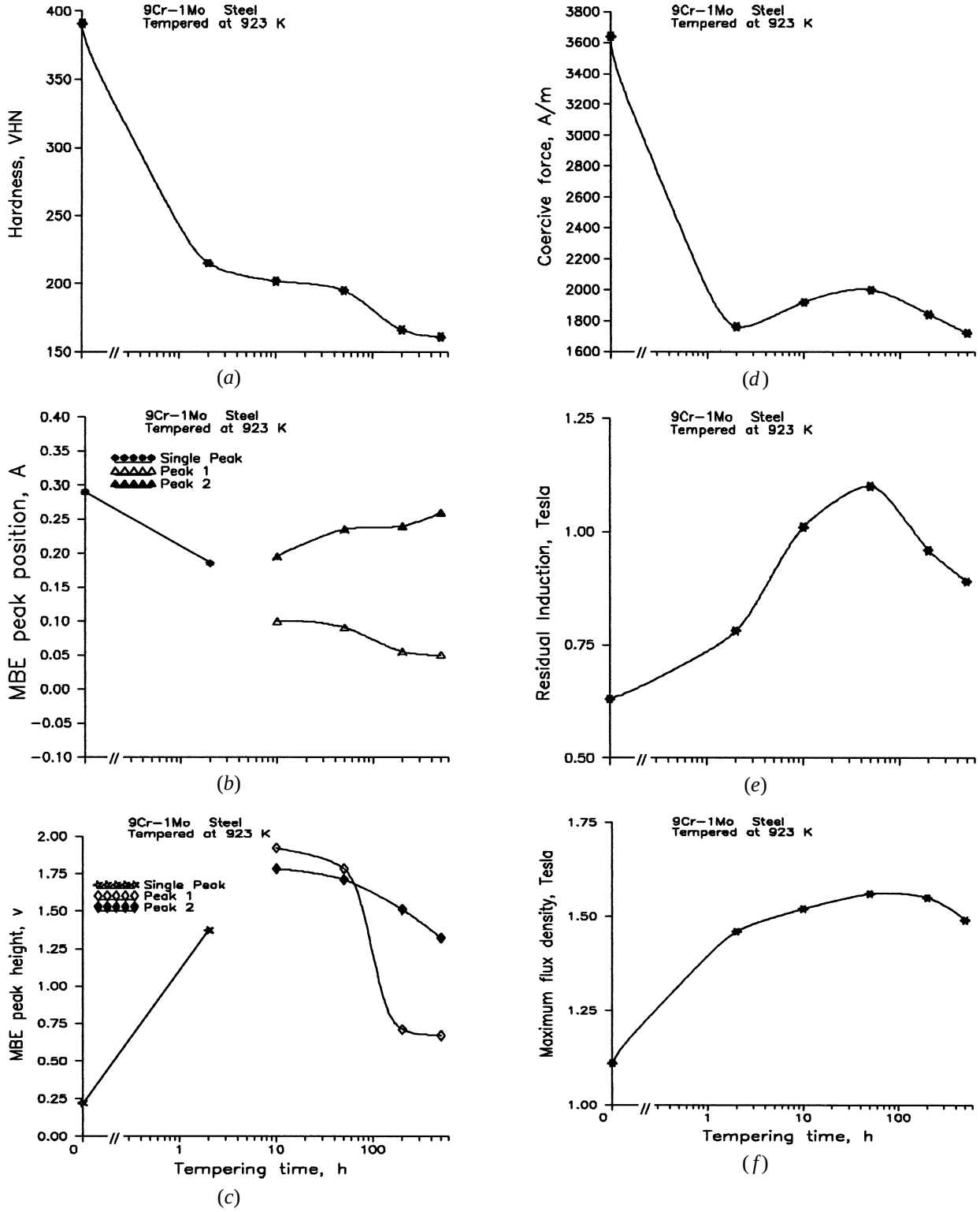


Fig. 9—The variation in (*a*) hardness, (*b*) MBE peak 1 and peak 2 positions, (*c*) MBE peak 1 and peak 2 height values, (*d*) coercive force ($H_c$), (*e*) residual induction ($B_r$), and (*f*) maximum flux density ($B_{max}$) as a function of tempering time for 9Cr-1Mo steel.

cess.[15,16] The initially observed single-peak MBE has been attributed to the presence of high dislocation density, which smears the individual effect of lath/grain boundaries and fine precipitates. Once the dislocation density assumes an equilibrium value, only the lath/grain size and precipitates size vary with tempering time. Considering the fact that the lath/grain boundaries and precipitates are the two major obstacles to the domain wall movement in sufficiently tempered microstructure, the MBE peak 1 at lower current applied to the yoke/magnetic field is attributed to the irre-

versible movement of domain walls existing at the ferrite lath/grain boundaries overcoming the grain boundary resistance. The MBE peak 2 at higher current is attributed to the irreversible movement of domain walls overcoming the resistance offered by the carbide precipitates.

a. *Effect of tempering on the MBE peak position*

The MBE peak position depends on the average pinning strength of the given type of obstacle. It can be observed from Figures 7(b), 8(b), and 9(b) that the MBE peak 1 position shifts to lower current/field, and the MBE peak 2 position moves to higher current with an increase in tempering time. It is evident from the micrographs (Figures 1(a) and (b), 3(a) and (b), and 5(a) and (b)) that the polygonization of ferrite laths and grain coarsening progress with tempering time. As the tempering progresses, the decrease in lath/grain boundary dislocation density and the closely related domain redistribution in the adjacent grains during polygonization would reduce the grain boundary magnetostatic energy, thereby reducing its resistance to domain wall motion. This results in the shifting of the MBE peak 1 position to lower field with an increase in tempering time. This is similar to the observation by Gatelier-Rothea *et al.*[25] in pure iron, who have also shown the shifting of the MBE peak position toward lower field with an increase in grain size. In Cr-Mo steels, the reduction in the MBE peak 1 position is delayed to longer tempering time as compared to carbon steel (Figures 7(b), 8(b), and 9(b)). This is because of the precipitation of fine $M_2X$ precipitates in Cr-Mo steels, which retard the lath/grain coarsening.[19–24] This is evident from the dense distribution of fine needle-like $M_2X$ precipitates even after 50 hours of tempering at 923 K (Figures 4(a) and 6(a)). However, after 500 hours (Figures 4(b) and 6(b)), the dissolution of needlelike $M_2X$ precipitates leads to faster lath coarsening and polygonization (Figures 3(b) and 5(b)) and, hence, the rapid reduction in the MBE peak 1 position.

It is evident from the micrographs (Figures 2(a) and (b), 4(a) and (b), and 6(a) and (b)) that the average carbide size increases with tempering time. The increase in carbide size increases the demagnetizing field associated with the magnetic free poles at the matrix-carbide interface and, hence, the pinning strength for domain wall movement.[26,27] This results in shifting of the MBE peak 2 position to higher current/field with an increase in tempering time (Figures 7(b), 8(b), and 9(b)).

b. *Quantification of average size of laths/grains and carbides from the MBE peak positions*

It has already been explained[15,16] that the MBE peak 1 is ascribed to the effect of grain boundaries and the peak 2 to that of precipitates. As explained previously, the variation in the peak position of the MBE from different sources would reflect the changes in the average size of the corresponding obstacles. Figure 10 shows the quantitative relation obtained between the MBE peak 1 position and average grain size for different tempered 0.2 pct carbon steel samples. Figure 11 shows a similar relation between the MBE peak 2 position and the average size of the cementite precipitates for the same steel. Excellent correlation between the MBE peak position and the microstructural parameters (Figures 10 and 11) clearly proves that the MBE technique can be used to evaluate the finer changes in the individual microstructural features.

The identification of two peaks clearly or at least slope

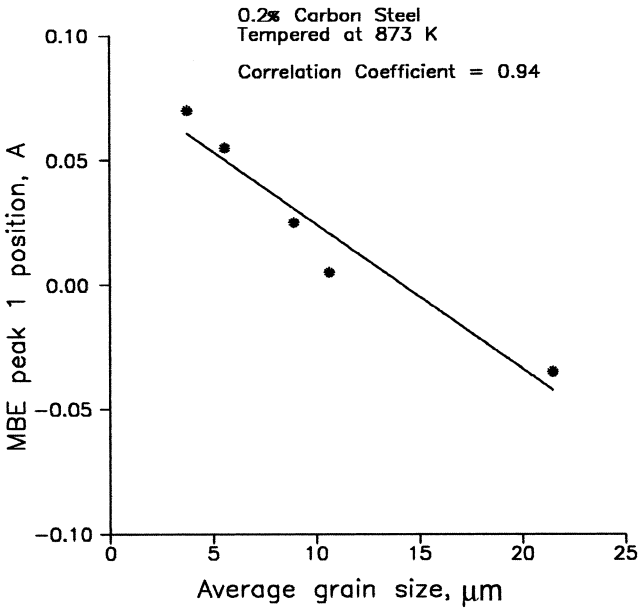


Fig. 10—Quantitative relation obtained between the MBE peak 1 position and average grain size for different tempered 0.2 pct carbon steel samples.

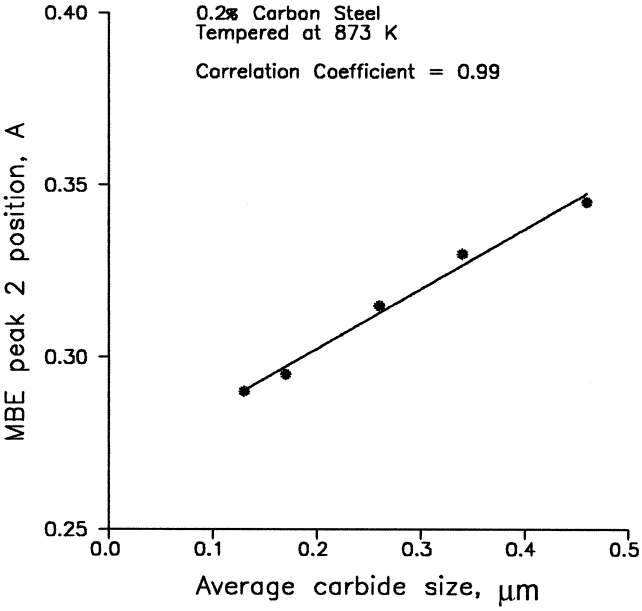


Fig. 11—Quantitative relation between the MBE peak 2 position and the average size of the cementite particles for different tempered 0.2 pct carbon steel samples.

changes in the MBE profile becomes possible only after a certain stage of tempering depending on the materials. This limits the determination of the average size of laths and carbides at short tempering times. However, the already obtained relationship between MBE peak position and the average size can be extrapolated for longer tempering times. Another important point to note here is that Figures 10 and 11 show the average lath/grain and carbide sizes that vary in a synergistic manner during tempering. Hence, such correlation has to be first established for different materials with the support of optical/electron microscopy. Later, they can be used as calibration standards for on-line assessment of components.

c. *Effect of tempering on the MBE peak height*

During magnetization, the RMS voltage level of the MBE at a given magnetic field depends on the number and the extent of the domain walls moving at a given instant. This, in turn, is decided by both the size distribution of the obstacle and the mean free path of the domain wall displacement. The size distribution decides the range of pinning strengths and, hence, the range of magnetic field strengths ($\Delta H$) in which the domain walls overcome a given type of obstacle. The narrower the size distribution (narrow $\Delta H$) and the larger the mean free path of the domain wall displacement, the greater is the MBE peak height.

It can be observed from Figures 7(c), 8(c), and 9(c) that, in all the three steels, both the MBE peak 1 and peak 2 height values reach a maximum and then fall with tempering time. The initial increase in the MBE peak 1 height has been attributed to the narrow size distribution of laths and the increase in the mean free path of the domain wall movement due to lath coarsening. As the grain size becomes coarser, the grain boundary area reduces and, hence, the number of reverse domain nucleation sites decreases.[25] This results in the reduction in the MBE peak 1 height at longer tempering times (Figures 7(c), 8(c), and 9(c)) even though the mean free path of the domain wall displacement increases. Similarly, the MBE peak 2 height shows a maximum corresponding to a narrow size distribution of carbides. As the carbide size increases with tempering time, the size distribution broadens, which, in turn, reduces the number of domain walls moving at a given instant. Thus, the MBE peak 2 height decreases with an increase in tempering time (Figures 7(c), 8(c), and 9(c)). Hence, the maximum MBE peak occurs when there is an optimum combination of size distribution and mean free path of the domain wall displacement. The maximum value of the MBE peaks occurs at an intermediate tempering time because of the fact that, at lower tempering time, the lower mean free path of the domain wall movement limits the MBE level. At higher tempering time, the reduction in the number of reverse domain nucleation sites due to coarse grain size and the broad size distribution limits the MBE level by reducing the number of domain walls moving at a given instant.

d. *Identification of dissolution of $M_2X$ precipitates in Cr-Mo steels*

In the case of carbon steel, the precipitation and growth of cementite precipitates result in the gradual reduction in both MBE peak height values (Figure 7(c)). However, in Cr-Mo steels, the precipitation of different types of carbides at different stages of tempering (transformation of carbides) leads to nonuniform variations in the MBE peak height values (Figures 8(c) and 9(c)). In Cr-Mo steels, there is a sharp drop in the peak 1 height after prolonged exposure (in 2.25Cr-1Mo steel after 500 hours Figure 8(c), and in 9Cr-1Mo steel after 200 hours Figure 9(c)). It has been shown in Figures 4(a) and 6(a) that, in both 2.25Cr-1Mo steel and 9Cr-1Mo steel, tempering at 923 K produces fine plate-type $M_2X$ precipitates densely distributed within the matrix. Being fine, the $M_2X$ precipitates would not be strong barriers to domain wall motion unlike the other larger size carbides such as $Fe_3C$, $Cr_7C_3$, $M_{23}C_6$, *etc.*, observed in these steels. However, it has been observed that their presence strongly retards the coarsening of ferrite laths,[19–24] and the dissolution of $M_2C$ or $M_2X$ in long-term tempered samples marks the rapid polygonization and growth of the ferrite grains (Figures 3(a) and (b) through 6(a) and (b)). This, in turn, would lead to a decrease in the boundary surface area and, hence, the number of reverse domain walls nucleating at the grain boundary. The rapid decrease in the peak 1 height values after 500 hours of tempering in 2.25Cr-1Mo and after 200 hours of tempering in 9Cr-1Mo steels (Figures 8(c) and 9(c)) can be considered as an indication of the dissolution of $M_2C$ or $M_2X$ precipitates. Similarly, in the case of 9Cr-1Mo steel also, the drastic reduction in the peak 2 height after 200 hours of tempering shows the rapid growth of $M_{23}C_6$ caused by the dissolution of $M_2X$ (Figure 9(c)).

It is interesting to note from Figures 8(c) and 9(c) that, in long-term tempered samples of Cr-Mo steels, the drastic reduction in the peak 2 height coincides with that in the peak 1 height (200 to 500 hours in the case of 2.25Cr-1Mo steel and 50 to 200 hours in the case of 9Cr-1Mo steel). This confirms the earlier mentioned explanation that the dissolution of $Mo_2C$ or $M_2X$ precipitates causes the rapid growth of both the ferrite grains and $M_{23}C_6$ precipitates, resulting in the drastic reduction in both the MBE peak heights in the Cr-Mo steels. The rapid and simultaneous reduction in both the MBE peak heights can be considered as an indication for the deterioration in the creep strength in these Cr-Mo steels.

3. *Effect of tempering on the hysteresis loop parameters*

a. *Effect of tempering on the coercive force, $H_c$*

It can be observed from Figures 7(d), 8(d), and 9(d) that, in all the steels, the coercive force drops rapidly after initial short tempering. This is attributed to the sharp reduction in the dislocation density that dominates the as-quenched microstructure. On further tempering, $H_c$ increases again and goes through a maximum. Long-term tempering leads to a gradual decrease in $H_c$. This nonlinear variation in $H_c$ with tempering time clearly shows that it cannot be related linearly with hardness. This is because the hardness is strongly decided by the coherency strain produced by the precipitates in the matrix. It is known that, for maintaining the lattice coherency, the precipitate size should be very small (few hundreds of *A*). As the precipitate grows, it loses coherency and leads to a drop in hardness. As far as the magnetic domain wall pinning strength is concerned, it does not matter whether the precipitate is coherent, because the pinning strength depends on the magnetostatic energy, which in turn, depends on the precipitate size. Also, maximum domain wall pinning strength would occur when the precipitate size would be of the same order as domain wall thickness ($\sim$1000 A)[26,27] which is much higher than that of the coherent particles.

During a magnetization cycle, the majority of the magnetization and demagnetization occur by the movement of reverse domain walls. Hence, it can be considered that the coercive force ($H_c$) is the magnetic field required for attaining the demagnetized condition where the entire volume of the sample can be divided into two halves, each having magnetic domains oriented 180 deg opposite. The extent of demagnetization at a given field on reducing the applied magnetic field from a maximum depends on the resistance of the obstacles to domain wall movement and the interobstacle spacing.

It has been shown earlier by the authors[15,16] that, when

the applied magnetic field is varied from $-H_{max}$ (−12,000 A/m) and $+H_{max}$ (+12,000 A/m), the magnetization process in tempered ferritic steels occurs in two stages; that is, on reducing the field from $-H_{max}$, the already existing reverse domain walls at lath/grain boundaries start moving away from the boundaries (stage 1), and on the way, they are pinned by the precipitates. On reversing and increasing the applied magnetic field toward $+H_{max}$, the domain walls overcome the precipitates at higher field (stage 2). Hence, the $H_c$ value depends on the pinning strengths of both the lath/grain boundaries and the carbide particles.

Figures 12(a) through (c) show the variations in the RMS voltage of the MBE, applied magnetic field, tangential magnetic field measured on the surface of the specimen, and the magnetic flux density as a function of the current applied to the yoke for half the magnetization cycle for all the three steels in the long-term tempered condition. It can be observed from Figures 12(a) through (c) that the $H_c$ point in the hysteresis curve corresponds to the trough between the MBE peak 1 and peak 2; that is, the $H_c$ point occurs in between the stage 1 and stage 2 magnetization process mentioned previously. This supports the previously mentioned fact that the $H_c$ value depends on the changes in the pinning strength of both grain boundaries and carbides. It can be observed from Figures 12(a) through (c) that the stage 1 process contributes more to demagnetization. However, the overlapping of stages 1 and 2 would result in the partial influence of the stage 2 on the $H_c$ value. Hence, the $H_c$ value for a given tempered microstructure is decided by the extent of both these stages, and the individual influence of grain boundaries and precipitates cannot be separated.

After short tempering, the dense distribution of carbide particles would pin the lath boundaries and resist polygonization. This effect tends to slow down the rate of reduction in the resistance of the lath boundaries to domain wall motion. The dense distribution of carbide particles also reduces the mean free path of the domain-wall displacement during stage 1. The increase in the size of the carbides also results in the increased resistance to domain-wall movement and would delay the starting of stage 2. Therefore, the net effect would be the increase in the overall resistance offered by the obstacles to domain wall movement, that is, a higher magnetic field would be required to achieve the demagnetized state. This results in the increase in $H_c$ value once again after the initial drop due to annihilation of dislocations. On prolonged tempering, the polygonization of ferrite laths would result in the easier movement of domain walls from the grain boundaries. The coarsening of carbide particles by the dissolution of smaller particles results in the reduction of the number density of precipitates and broader size distribution (Figures 2(a) and (b), 4(a) and (b), and 6(a) and (b)). The resistance offered by very fine particles can easily be overcome by the domain walls. Also, some of the large-size carbides (>0.5 $\mu$m) would tend to have closure/spike domains around them, thereby reducing their magnetostatic energy and, hence, their resistance to domain-wall motion.[26,27] This would lead to the increase in the domain-wall displacement during stage 1 and the early starting of stage 2. Therefore, in long-term tempered samples, there is a net reduction of the overall resistance to domain wall movement, which results in a continuous decrease in the $H_c$ value with tempering time (Figures 7(d), 8(d), and 9(d)).

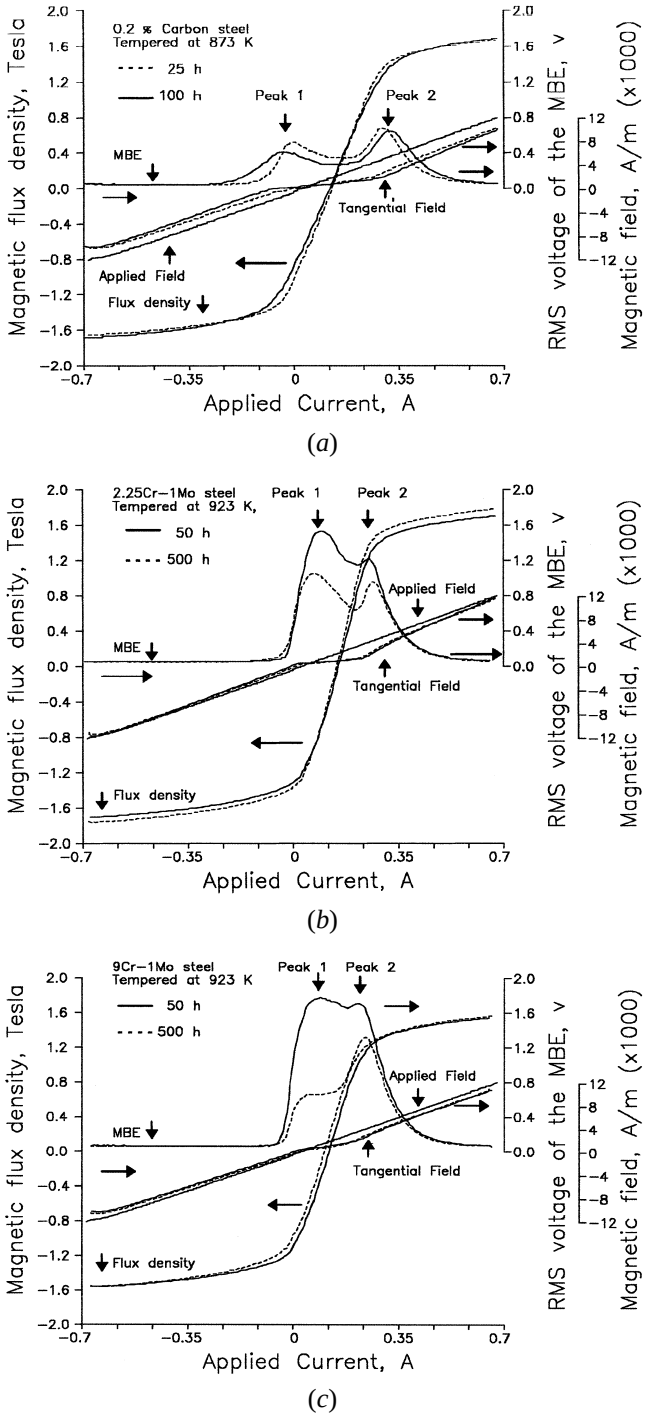


Fig. 12—The typical variations in the RMS voltage of the MBE, applied magnetic field at the center of the pole pieces in the absence of the specimen, tangential magnetic field measured on the surface of the specimen, and the magnetic flux density as a function of current applied to the yoke for half the magnetization cycle for (*a*) 0.2 pct carbon steel, (*b*) 2.25Cr-1Mo steel, and (*c*) 9Cr-1Mo steel samples in long-term tempered condition.

b. *Effect of tempering on the residual induction, $B_r$*

It can be observed from Figures 7(e), 8(e), and 9(e) that the residual induction ($B_r$) initially increases slowly and then more rapidly after short tempering. The $B_r$ reaches a maximum and then decreases on prolonged tempering. The $B_r$ value indicates the extent of demagnetization before reversing the magnetic field, which, in turn, is decided by

the displacement of reverse domain walls. Hence, the extent of demagnetization depends on the resistance of the obstacles to domain wall movement and the interobstacle spacing. It can be observed from Figures 12(a) through (c) that the $B_r$ coincides more or less with the MBE peak 1. This shows that the $B_r$ is decided by the extent of domain-wall movement during stage 1 magnetization process; that is, the $B_r$ value is more influenced by the effect of lath/grain boundaries.

The $B_r$ is strongly influenced by the magnetic anisotropy of the microstructure. In the case of quenched microstructure, each lath can be considered as a single domain (owing to their smallness). The complex magnetic anisotropy with a large demagnetizing field results in reversible domain alignment in small localized regions during magnetization. Hence, on reducing the magnetic field, a large amount of reversible domain alignment results in a rapid demagnetization leading to a low $B_r$ value. However, the coarsening of the laths on tempering slowly transforms the single domain structure of the laths into a multidomain structure. Also, the precipitation of secondary phases at the lath boundaries and at the lath interior during tempering enhances the irreversibility of the domain wall motion. Hence, the magnetization process changes from the reversible domain alignment in quenched samples to irreversible domain wall movement in tempered samples. This causes the increase in the $B_r$ value after tempering.

The initial tempering results in the reduction in dislocation density and partial transformation of martensite/bainite to ferrite. This results in a slow rise in the $B_r$ value. During tempering, the second-phase precipitation initially results in a fine, dense distribution of carbides (Figures 2(a), 4(a), and 6(a)). The high number density of carbide particles (small interobstacles spacing) after short tempering restricts the domain-wall displacement from the lath/grain boundaries. The restricted domain-wall displacement and the enhancing irreversibility result in the sharp rise in the $B_r$ value with tempering time. On prolonged tempering, the grain coarsening and the reduction in the number density of second-phase particles due to coarsening result in large interobstacle spacing (Figures 2(b), 4(b), and 6(b)). Hence, there is an increase in the extent of domain wall displacement during stage 1 magnetization. This results in a decrease in the $B_r$ value with tempering time in long-term tempered samples.

It can be noted from Figures 7 through 9 that the maximum in $B_r$ value and the $H_c$ value occur at the same tempering time in all the three steels. This clearly shows that the hysteresis loop parameters are decided by the changes in the overall resistance of the obstacles to domain wall movement, that is to the pinning strengths of both the lath/grain boundaries and the second-phase particles and the interobstacle spacing in tempered samples.

c. *Effect of tempering on the maximum flux density, $B_{max}$*

It can be observed from Figures 7(f), 8(f), and 9(f) that, with an increase in tempering time, the $B_{max}$ value also increases to a maximum and then decreases in all the three steels. The initial increase in the $B_{max}$ value with tempering time indicates the softening of the microstructure, which facilitates the movement of the domain walls. Due to the precipitation of the second phases, the removal of alloying elements such as Cr, Mo, *etc*., from the matrix also contributes to the increase in the $B_{max}$ value. On prolonged tempering, as the average sizes of the grains and carbides increase, the magnetic-free pole density and the demagnetizing field associated with them also increase. The increasing demagnetizing field can easily form reverse spike domains at the grain boundaries. The demagnetizing field at some of the large-size carbide particles ($>0.5$ $\mu$m) would also form 90 deg closure spike domains. The formation of such residual spike domains at the microstructural features in order to reduce the local magnetostatic energy would contribute to the small reduction in $B_{max}$ value in long-term tempered samples.

## IV. CONCLUSIONS

This study establishes the fact that the MBE is very sensitive to fine microstructural changes during different stages of tempering in ferritic steels. It has been shown that the changes in the lath/grain size and carbide size can be individually characterized using MBE; that is, the variations in the size and distribution of laths/grains caused by tempering at high temperature can be quantified from the MBE peak 1 and those of second-phase precipitates from the MBE peak 2. Such individual variations in the microstructural features cannot be identified and quantified by the $H_c$ and $B_r$, because they are influenced by the synergistic changes in the microstructural features. The quantitative relationships between the MBE parameters and the microstructural parameters, once established with the actual information from optical/electron microscopy for different ferromagnetic materials, can be used for evaluating the microstructural state in the as-fabricated and service exposed components.

## ACKNOWLEDGMENTS

We are thankful to Mrs. M. Vijayalakshmi and Mrs. Saroja Saibaba, Scientists, Physical Metallurgy Section, for their useful discussions and support during TEM investigation. We are also thankful to Mr. P. Kalyanasundaram, Head, Division for PIE and NDT Development, for his keen interest and to Dr. Placid Rodriguez, Director, Indira Gandhi Centre for Atomic Research (Kalpakkam), for his encouragement and support.

## REFERENCES

1. M.N. Mikheev and E.S. Gorkunov: *Sov. J. NDT*, 1981, vol. 17 (8), pp. 579-662.
2. E.S. Gorkunov: *Sov. J. NDT*, 4 (1991) 231-59.
3. S. Tiitto: *Acta Polytechnica Scandinavica, Applied Physics Series No. 119*, Helsinki, Finland, 1977, pp. 1-80.
4. G.A. Matzkanin, R.E. Beissner, and C.M. Teller: "The Barkhausen effect and its applications to Nondestructive evaluation," Report No. NTIAC-79-2, Southwest Research Institute, San Antonio, TX, 1979, pp. 1-49.
5. F. Vitsena: *Chekhosl. Fiz. Z.*, 5(4) (1955) 480-501.
6. G. Trauble and A. Zeger: *Plastic Deformation of Single Crystals*, Mir, Moscow, 1969, pp. 201-64.
7. T.D. Yensen and N.A. Ziegler: *Trans. ASM*, 23 (1935) 556-57.
8. W.E. Rieder: *Trans. ASM*, 22 (11)(1934) 1120-41.
9. M. Kersten: *Z. Phy.*, 124 (1948) 714-42.
10. D.L. Dijkstra and C. Wert: *Phy. Rev.*, 79 (6) (1950) 979-85.
11. J.B. Goodenough: *Phy. Rev.*, 95(4) (1954) 917-32.
12. L. Neel: *Cah. Phys.*, 25 (1944) 21-44.
13. S.V. Vonsovskii: *Magnetism*, Nauka, Moscow, 1971, pp. 835-52.

14. S.K. Ray and O.N. Mohanty: *J. Magn. Magn. Mater.*, 78 (1989) 255-62.
15. V. Moorthy, S. Vaidyanathan, T. Jayakumar, and Baldev Raj: *J. Magn. Magn. Mater.*, 1997, vol. 171, pp. 179-89.
16. V. Moorthy, S. Vaidyanathan, T. Jayakumar, and Baldev Raj: *Phil. Mag. A*, 77 (6) (1998) 1499-1514.
17. G.R. Speich: *Trans. TMS-AIME*, 245 (1969) 2553-64.
18. R.N. Caron and G. Krauss: *Metall. Trans.*, 3 (1972) 2381-89.
19. R.C. Baker and J. Nutting: *J. Iron Steel Inst., London*, 7 (1959) 257-68.
20. P. Parameswaran, M. Vijayalakshmi, P. Shankar, and V.S. Raghunathan: *J. Mater. Sci.*, 27 (1992) 5426-34.
21. J. Orr, F.R. Beckitt, A. Met, and G.D. Fawkes: *Proc. Int. Conf. Ferritic Steels for Fast Reactors Steam Generators*, S.F. Pugh and E.A. Little, eds., British Nuclear Energy Society, London, 1978, pp. 91-109.
22. S.J. Sanderson: *Proc. Int. Conf. Ferritic Steels for Fast Reactors Steam Generators*, S.F. Pugh and E.A. Little, eds., British Nuclear Energy Society, London, 1978, pp. 120-27.
23. S. Saroja, P. Parameswaran, M. Vijayalakshmi, and V.S. Raghunathan: *Acta Metall.*, 43 (8) (1995) 2985-3000.
24. S. Saroja, M. Vijayalakshmi, and V.S. Raghunathan: *Mater. Trans. JIM*, 34 (10) (1993) 901-06.
25. C. Gatelier-Rothea, P. Fleishmann, J. Chicois, and F. Fourgeres: *Non-destr. Testing Eval.*, 1992, No. 8–9, pp. 591-602.
26. R.S. Tebble and D.J. Craik: *Magnetic Materials*, Wiley Interscience, New York, NY, 1969, pp. 369-411.
27. B.D. Cullity: *Introduction to Magnetic Materials*, Addison-Wesley, Reading, MA, 1972, p. 292.